Equatorial Circulation of a Global Ocean Climate Model with Anisotropic Horizontal Viscosity

WILLIAM G. LARGE, GOKHAN DANABASOGLU, JAMES C. MCWILLIAMS, PETER R. GENT, AND FRANK O. BRYAN

National Center for Atmospheric Research, Boulder, Colorado

(Manuscript received 6 August 1999, in final form 3 May 2000)

ABSTRACT

Horizontal momentum flux in a global ocean climate model is formulated as an anisotropic viscosity with two spatially varying coefficients. This friction can be made purely dissipative, does not produce unphysical torques, and satisfies the symmetry conditions required of the Reynolds stress tensor. The two primary design criteria are to have viscosity at values appropriate for the parameterization of missing mesoscale eddies wherever possible and to use other values only where required by the numerics. These other viscosities control numerical noise from advection and generate western boundary currents that are wide enough to be resolved by the coarse grid of the model. Noise on the model gridscale is tolerated provided its amplitude is less than about 0.05 cm s^{-1}. Parameter tuning is minimized by applying physical and numerical principles. The potential value of this line of model development is demonstrated by comparison with equatorial ocean observations.

In particular, the goal of producing model equatorial ocean currents comparable to observations was achieved in the Pacific Ocean. The Equatorial Undercurrent reaches a maximum magnitude of nearly 100 cm s^{-1} in the annual mean. Also, the spatial distribution of near-surface currents compares favorably with observations from the Global Drifter Program. The exceptions are off the equator; in the model the North Equatorial Countercurrent is improved, but still too weak, and the northward flow along the coast of South America may be too shallow. Equatorial Pacific upwelling has a realistic pattern and its magnitude is of the same order as diagnostic model estimates. The necessary ingredients to achieve these results are wind forcing based on satellite scatterometry, a background vertical viscosity no greater than about 1 cm^2 s^{-1}, and a mesoscale eddy viscosity of order 1000 m^2 s^{-1} acting on meridional shear of zonal momentum. Model resolution is not critical, provided these three elements remain unaltered. Thus, if the scatterometer winds are accurate, the model results are consistent with observational estimates of these two coefficients. These winds have larger westward stress than NCEP reanalysis winds, produce a 14% stronger EUC, more upwelling, but a weaker westward surface flow.

In the Indian Ocean the seasonal cycle of equatorial currents does not appear to be overly attenuated by the horizontal viscosity, with differences from observations attributable to interannual variability. However, in the Atlantic, the numerics still require too large a meridional viscosity over too much of the basin, and a zonal resolution approaching 1° may be necessary to match observations. Because of this viscosity, increasing the background vertical viscosity slowed the westward surface current; opposite to the response in the Pacific.

1. Introduction

Equatorial ocean regions play a fundamental role in the earth's climate. In the tropical Atlantic, climate variability, including precipitation in adjacent continental regions, has been related to the hemispheric gradient in sea surface temperature (SST) (Hastenrath 1991; Carton et al. 1996). The Asian–Australian monsoon has been found to affect global as well as regional climate on seasonal timescales, with suggestions of a role for Indian and Pacific equatorial SST (Webster et al. 1998). Of course, the strongest and most predictable feature of interannual climate variability is the El Niño–Southern Oscillation (ENSO) phenomenon that is characterized by SST anomalies in the central and eastern equatorial Pacific. Describing the time-varying tropical Pacific Ocean, understanding the physical mechanisms of ENSO, and determining the associated predictability were among the objectives of the Tropical Ocean–Global Atmosphere (TOGA) program. The success of TOGA is documented in a series of review papers in a 1998 special issue of the *Journal of Geophysical Research* (Vol. 103, No. C7). An earlier view of ENSO and other features of equatorial air–sea interaction are comprehensively discussed in Philander (1990).

Many investigations of these phenomena rely on ocean general circulation models (Stockdale et al. 1998), which are sometimes coupled to an atmosphere (Delecluse et al. 1998; Biasutti and Battisti 2001). For process

Corresponding author address: Dr. William G. Large, NCAR, P.O. Box 3000, Boulder, CO 80307.
E-mail: wily@ncar.ucar.edu.

studies (e.g., Chen et al. 1994a) and prediction purposes (Latif et al. 1998) of relevance to TOGA, it is possible to use relatively high-resolution ocean models (e.g., Philander et al. 1987), by either keeping the integration times short and/or using regional ocean domains. These options are not available when modeling past and future climate changes because of the very long (thousands of years) timescales and the global nature of the problem.

Equatorial ocean dynamics are unique because of the vanishing Coriolis force (Gill 1982). The dominant zonal momentum balance is between the wind, a pressure gradient, and advection. However, residual imbalances accelerate a downwind (usually westward) flow near the surface and an eastward Equatorial Undercurrent (EUC) to the point where momentum flux divergences make up the differences (Wacongne 1989). The challenge for climate modeling is to reliably parameterize these momentum fluxes. The issue of equatorial vertical momentum exchange has been addressed in many works, with different schemes introduced by Pacanowski and Philander (1981), Rosati and Miyakoda (1988), Gent and Cane (1989), Schudlich and Price (1992), Chen et al. (1994b), and Large and Gent (1999).

Less attention has been given to the very different problem of horizontal momentum fluxes, where numerical considerations (Bryan et al. 1975) are more important but compromise physical realism (McWilliams 1996). Usually there is a local downgradient flux with a single (isotropic) constant eddy coefficient. Maes et al. (1997) found that varying such a coefficient by three orders of magnitude had little effect on equatorial SST, but changed currents a great deal. At the other end of the spectrum in complexity are schemes based on Smagorinsky (1963), where the eddy coefficient depends on the time evolving, spatially varying flow as well as the grid spacing. The basis of this viscosity is three-dimensional, homogeneous, isotropic turbulence and it has proved very useful in models of such flows (e.g., large eddy simulations). It was first applied to two-dimensional turbulence in atmospheric models with resolved baroclinic eddies. It may not, however, be appropriate for ocean climate models where there is neither isotropic, nor homogeneous turbulence, nor resolved eddies. Nonetheless, Rosati and Miyakoda (1988) and Miller et al. (1992) employ such schemes in large-scale models, but both use anisotropic viscosity in such a way that the friction introduces unphysical torques (Wajsowicz 1993). Pacanowski and Griffies (1998) present a physically consistent implementation using only a single, spatially varying coefficient and Griffies and Hallberg (2000) extend this for use in eddy-permitting ocean models.

An alternative, physically consistent, anisotropic horizontal viscosity is proposed in section 2. Only a limited subset of possible ways of specifying the two, spatially varying viscosity coefficients has been explored. The guiding principle is that these coefficients be physically based wherever possible, given their necessary role in controlling solution variance (numerical noise) on the grid scale. The result is a reasonable parameterization of the viscous effects of mesoscale eddies in the equatorial oceans that allows advective and wave dynamics to be as active as possible in one particular model. Modifications may be necessary when applied to other ocean regions, or differently constructed models. The overall performance is tested in a series of numerical experiments that are described in section 3. In section 4 the best solution is compared to observations, mostly in the Pacific sector where the longest and most complete datasets have been compiled. The main data source is the TOGA observing system (McPhaden et al. 1998), which includes the Tropical Atmosphere–Ocean (TAO) moored array and the Global Drifter Program. Model sensitivities to anisotropic versus isotropic horizontal viscosity, to the wind forcing, and to internal wave mixing are presented in section 5. Section 6 contains general discussion and overall conclusions.

2. Anisotropic horizontal viscosity

Global ocean climate models by necessity have coarse horizontal resolution (usually fewer than the 64 000 grid points of a 1° model). Two such examples are the nominal 3° (100° longitude by 74° latitude) resolution described in Large et al. (1997) and its 2° (150 by 111) partner (Gent et al. 1998). They have 25 and 45 vertical levels, respectively, and are our previous configurations of the Climate System Model ocean component, which is adapted from the Modular Ocean Model 1.1 (Bryan 1969; Pacanowski et al. 1991, 1993). One of the serious deficiencies of both their solutions is their equatorial ocean circulation. Most obvious is the overly broad and weak EUC, whose maximum zonal velocity (10 cm s^{-1}) is only about 10% of the observed.

One step in an attempt to overcome this shortcoming, especially in the Pacific where there is the strongest coupling to atmospheric climate, has been to enhance the meridional resolution in the Tropics. The refined 2° and 3° configurations, respectively, have constant 0.6° and 0.9° meridional grid spacing between 10°N and 10°S, have a total of 173 and 116 latitudes, place 4 and 3 levels in the upper 50 m, and are referred to as the $\times 2'$ and $\times 3'$ models, respectively. A more important step is the following reformulation of the horizontal momentum flux divergences, F_H^u and F_H^v. We retain an eddy-viscosity parameterization, but the viscosity is anisotropic. In this first implementation the coefficients are variable in space, but constant in time. Although the currents in both $\times 2'$ and $\times 3'$ are generally too broad and sluggish, we will show below that the zonal equatorial currents become much more realistic when there is a small, physically based eddy viscosity in the cross-stream (meridional) direction.

The model dynamics are governed by the primitive equations in spherical coordinates (λ, ϕ, z) for an earth of mean radius a, gravitational acceleration g, and an-

gular velocity Ω, with hydrostatic, Boussinesq, and rigid-lid approximations:

$$u_t + \mathcal{L}(u) - \left(f + \frac{u\tan\phi}{a}\right)v = -\left(\frac{1}{a\cos\phi}\right)\left(\frac{p}{\rho_0}\right)_\lambda + F_H^u + F_V^u, \quad (1a)$$

$$v_t + \mathcal{L}(v) + \left(f + \frac{u\tan\phi}{a}\right)u = -\frac{1}{a}\left(\frac{p}{\rho_0}\right)_\phi + F_H^v + F_V^v, \quad (1b)$$

$$p_z = -\rho g, \quad (1c)$$

$$\left(\frac{1}{a\cos\phi}\right)[u_\lambda + (v\cos\phi)_\phi] + w_z = 0. \quad (1d)$$

In (1), u, v, and w are the longitudinal (λ), latitudinal (ϕ), and vertical (z) velocity components, respectively, t is time, p is pressure, ρ is density, ρ_0 (=1000 kg m^{-3}) is the reference density and $f = 2\Omega\sin\phi$ is the Coriolis parameter. The vertical momentum flux divergences are F_V^u and F_V^v. Partial derivatives with respect to independent variables are denoted by subscripts; $\mathcal{L}$ is the advection operator,

$$\mathcal{L}(G) = \left(\frac{1}{a\cos\phi}\right)[(uG)_\lambda + (vG\cos\phi)_\phi] + (wG)_z, \quad (2)$$

where G is either u or v.

Following common practice, the ratio of vertical to horizontal eddy viscosities in the ocean interior is between 10^{-7} and 10^{-10}. This anisotropy reflects the fact that the vertical and horizontal mixing processes being parameterized are different. However, for both physical and computational reasons, we deviate from standard practice of transverse isotropy and have two spatially varying horizontal viscosity coefficients. The physical motivation for this anisotropy is the prevalence of strong ocean currents that vary more sharply in the cross-stream direction. Also, the axes of material fronts lie along the mean flow direction because the transport of material properties, and probably momentum, is more efficient along the flow direction than across it. These observations suggest that different processes may operate in the two directions and that excess cross-stream viscosity would overly broaden such currents and diffuse the material fronts. The computational reason is that the grid spacing is usually spatially variable and anisotropic and, because horizontal viscosities need be no larger than necessary to achieve smooth solutions on the grid scale, it may be advantageous for them to have these properties too. Of course, insofar as the model grid scale exceeds the true physical width of a current, minimizing the cross-stream eddy viscosity limits the magnitude of the model bias.

Eddy viscosity arises from a parameterization of the deviatoric component, $\mathbf{d}$, of the Reynolds stress, $\boldsymbol{\sigma}$, as proportional to the shear of the resolved flow, $\mathbf{u}$, where $\mathbf{d}$ must have zero trace (Batchelor 1967; Miles 1994). The most general form of this relation in orthogonal, curvilinear coordinates is

$$\sigma_{ij} \equiv -\overline{u_i' u_j'} = -\frac{1}{3}\delta_{ij}\overline{u_k' u_k'} + d_{ij}, \qquad d_{ij} \equiv T_{ijkl}e_{kl},$$

$$e_{kl} \equiv \frac{1}{2}[\nabla_k u_l + \nabla_l u_k], \quad (3)$$

where the indices span {1, 2, 3}, summation is implied by index repetition, and ∇_i denotes differentiation with respect to the ith coordinate; $\mathbf{T}$ is a fourth-order tensor. For physical realizability of the stress tensor it must satisfy symmetry of $\boldsymbol{\sigma}$ and $\mathbf{d}$, and $\mathbf{d} = 0$ for a $\mathbf{u}$ expressing uniform rotation about any axis. These conditions were described by Love (1944) and, more recently in the context of atmospheric and ocean motions with transverse isotropy, by Williams (1972) and, for spatially varying viscosity, by Wajsowicz (1993). They, together with the second-order differentiability of the dissipation function, $\mathcal{D} \equiv \mathbf{e} : \mathbf{T} : \mathbf{e}$, lead to the symmetries

$$T_{ijkl} = T_{jikl} = T_{ijlk} = T_{klij}, \quad (4)$$

which imply that of the $3^4 = 81$ elements of $\mathbf{T}$, only 21 are independent.

The state of the art of oceanic parameterization is not yet sophisticated enough to allow a sensible specification of so many independent parameters in $\mathbf{T}$. Therefore, we seek a minimal, anisotropic representation, in which the deviatoric stress divergence, $\nabla_i d_{ij}$, has only second derivatives operating on u_j, without any cross-coordinate derivatives or cross-component terms, in the special case of Cartesian coordinates with spatially uniform but anisotropic eddy viscosities. Our rationale for this choice is its similarity to the familiar isotropic form with a single, constant eddy viscosity, A, such that $\nabla_i d_{ij} = A\nabla^2 u_j$. One way this can be achieved in general orthogonal curvilinear coordinates is with only three independent parameters (i.e., viscosity coefficients), which have arbitrary space–time dependence, and the following definitions:

$$\begin{aligned} T_{1111} &= T_{2222} = A_{MH} + B_{MH}, \\ T_{3333} &= A_{MH} + A_{MV}, \\ T_{1212} &= B_{MH}, \\ T_{1313} &= T_{2323} = A_{MV}, \\ T_{1133} &= T_{2233} = B_{MH} - A_{MV}, \end{aligned} \quad (5)$$

where all other coefficients in $\mathbf{T}$, not related to these by the symmetries (4), are taken to be zero. For a 3D incompressible flow with $\nabla \cdot \mathbf{u} = \mathrm{tr}[\mathbf{e}] = 0$, one can verify that (5) assures $\mathrm{tr}[\mathbf{d}] = 0$ and becomes equivalent to the transverse isotropy specification of Wajsowicz (1993) when $A_{MH} = B_{MH}$.

A simple illustration of (5) is spatially uniform, nonnegative $\{A_{MH}, B_{MH}, A_{MV}\}$ in Cartesian coordinates:

$$F_H^u + F_V^u = \hat{\mathbf{x}} \cdot \boldsymbol{\nabla} \cdot \mathbf{d} = A_{MH} u_{xx} + B_{MH} u_{yy} + A_{MV} u_{zz},$$
$$F_H^v + F_V^v = \hat{\mathbf{y}} \cdot \boldsymbol{\nabla} \cdot \mathbf{d} = B_{MH} v_{xx} + A_{MH} v_{yy} + A_{MV} v_{zz}. \quad (6)$$

The quantity A_{MV} is recognizable as the vertical viscosity, while there are two horizontal viscosities, A_{MH} and B_{MH}. The latter operates in the cross-stream direction of each horizontal component, and A_{MH} operates in the downstream direction.

More relevant to global-scale ocean models is spatially variable $\{A_{MH}, B_{MH}, A_{MV}\} \geq 0$ in the thin spherical coordinates of (1). From (5) the momentum flux divergences become

$$\begin{aligned} F_H^u = {} & \frac{1}{a^2 \cos^2\phi}(A_{MH} u_\lambda)_\lambda + \frac{1}{a^2 \cos\phi}(B_{MH} \cos\phi u_\phi)_\phi \\ & + \frac{(1 - \tan^2\phi)}{a^2} B_{MH} u - (A_{MH} + B_{MH}) \frac{\tan\phi}{a^2 \cos\phi} v_\lambda \\ & + \left[\frac{\tan\phi}{a^2} u + \frac{v_\lambda}{a^2 \cos\phi}\right](B_{MH})_\phi - \frac{\tan\phi}{a^2 \cos\phi} v (A_{MH})_\lambda \\ & - \frac{v_\phi}{a \cos\phi}(B_{MH})_\lambda, \end{aligned} \quad (7)$$

$$\begin{aligned} F_H^v = {} & \frac{1}{a^2 \cos^2\phi}(B_{MH} v_\lambda)_\lambda + \frac{1}{a^2 \cos\phi}(A_{MH} \cos\phi v_\phi)_\phi \\ & + \frac{(B_{MH} - \tan^2\phi A_{MH})}{a^2} v + (A_{MH} + B_{MH}) \frac{\tan\phi}{a^2 \cos\phi} u_\lambda \\ & + \left[\frac{\tan\phi}{a^2} v - \frac{u_\lambda}{a^2 \cos\phi}\right](B_{MH})_\phi \\ & + \left[\frac{\tan\phi}{a^2 \cos\phi} u + \frac{u_\phi}{a^2 \cos\phi}\right](B_{MH})_\lambda, \end{aligned} \quad (8)$$

$$F_V^u = [A_{MV} u_z]_z, \quad (9)$$

$$F_V^v = [A_{MV} v_z]_z. \quad (10)$$

In certain special ocean regions, such as the core of the Antarctic Circumpolar Current, mesoscale eddies may not dissipate kinetic energy (McWilliams and Chow 1981). However, kinetic energy dissipation is required to be nonnegative-definite in the volume integral, which can be assured with local $\mathcal{D} \geq 0$ everywhere. In the Cartesian coordinates of (6) this condition is satisfied locally wherever $A_{MH}, B_{MH}, A_{MV} \geq 0$, for either the hydrostatic primitive equations (1), or the nonhydrostatic equations. In a more general orthogonal curvilinear system, including the spherical coordinates of (7)–(10), $A_{MH} \geq B_{MH}$ is an additional requirement, consistent with the physical motivation above to restrict the cross-stream momentum diffusion.

The lower bound for A_{HM} and B_{HM} in our eddyless ocean climate model is set to account for all the missing mesoscale eddy activity. An appropriate, approximate value indicated the rate of dispersion of neutrally buoyant floats in the ocean (Freeland et al. 1975; McWilliams et al. 1983) is $A_{\text{eddy}} = 1 \times 10^3 \text{ m}^2 \text{ s}^{-1}$.

Bryan et al. (1975) discuss two numerical constraints that require larger viscosity. First, the width of viscous western boundary layers (Munk 1950) must exceed the grid spacing in the offshore direction, Δx, which sets a criterion for viscosity

$$A_{\text{Munk}} > \left(\frac{\sqrt{3}}{\pi}\right)^3 \beta \Delta x^3, \quad (11)$$

where $\beta = f_\phi = 2.28 \cos\phi \times 10^{-11} \text{ m}^{-1} \text{ s}^{-1}$. It is this requirement that sets the viscosity in models with constant, isotropic formulations and horizontal grid spacings larger than about 1°. For example, in our previous configurations with $\Delta\lambda = 3.6°$ and 2.4°, (11) was satisfied with $A_{MH} = B_{MH} = 300 \times 10^3 \text{ m}^2 \text{ s}^{-1}$ and $80 \times 10^3 \text{ m}^2 \text{ s}^{-1}$, respectively.

Second, with centered differencing, the grid Reynolds number should be less than 2 so that numerical noise advected into a grid cell can be effectively diffused away. In one dimension, this consideration requires a viscosity

$$A_{\text{gre}} > \frac{1}{2} V \Delta, \quad (12)$$

where V and Δ are the velocity and grid spacing. However, it may not be necessary to satisfy (12) in all three dimensions (Weaver and Sarachik 1991). In previous implementations it is not satisfied everywhere in the vertical, but the noise is apparently controlled by the large horizontal viscosities required by (11). With anisotropic viscosity, this idea is carried further by assuming that it is sufficient to satisfy (12) in the alongstream direction only, by equating A_{MH} in (7) and (8) to the viscosity required by the larger grid spacing, with a lower limit set by A_{eddy}:

$$A_{MH}(\phi, z) = \max\left(\frac{1}{2} V(z) \Delta x(\phi), \frac{1}{2} V(z) \Delta y(\phi), A_{\text{eddy}}\right). \quad (13)$$

In (13) the spatial dependencies are given for our usual configuration of constant $\Delta\lambda$ and meridionally varying $\Delta\phi$. At present, the velocity in (13) is prescribed conservatively to satisfy expected equatorial currents, with $V_o = 100 \text{ cm s}^{-1}$:

$$V(z) = V_o e^{z/D}, \quad (14)$$

where the e-folding depth is $D = 1500$ m so that near the bottom $V(-4000 \text{ m}) = 7 \text{ cm s}^{-1}$.

Inspection of (7) and (8) reveals that B_{MH} operates on both $u_{\phi\phi}$ and $v_{\lambda\lambda}$. In the former, it needs to be a low, physically based value to allow equatorial currents to develop properly. In the latter it needs to be very much larger in order for the western boundary current to be

resolved. A solution to this dilemma is to assume that (11) needs to be satisfied by large viscosity only near western boundaries with continents, islands, and bottom topography given by

$$B_{\text{Munk}} = 0.2\beta\Delta x^3 e^{-p(x)^2}, \tag{15}$$

where $p(x)$ causes B_{Munk} to fall off as fast as possible away from boundaries. Numerous experiments of both $\times 2'$ and $\times 3'$ were performed in order to find an acceptable function and the empirical result is

$$p(x) = L_M^{-1} \max(0, x - x_N), \tag{16}$$

where x_N is the zonal coordinate of the Nth grid point east of the nearest western boundary. Viscosity is not similarly increased near zonal and eastern boundaries because doing so does not reduce numerical noise. The choice of length scale $L_M = 1000$ km and $N = 3$ is a compromise between maintaining current strengths in equatorial regions, with acceptable noise levels, but there is excessive noise in some high-latitude regions. Therefore, in order to make the global integrations useful for other purposes, this noise is controlled by increasing the mesoscale eddy viscosity away from the equator with

$$B_{\text{eddy}} = A_{\text{eddy}}[1 + 24.5(1 - \cos 2\phi)]. \tag{17}$$

Combining these considerations gives

$$B_{MH} = \max(B_{\text{Munk}}, B_{\text{eddy}}). \tag{18}$$

Finally, it must be ensured that momentum can neither diffuse nor advect through a grid cell in less than a model time step, Δt. The advective criterion leads to the familiar CFL limit (Bryan et al. 1975), which sets Δt. The diffusive criterion requires

$$A_{MH} + B_{MH} \le \frac{1}{4\Delta t} \min(\Delta x^2, \Delta y^2). \tag{19}$$

Generally, this constraint is not satisfied as Δx becomes small near the North Pole. In such regions both A_{MH} and B_{MH} are reduced by a common factor that makes (19) an equality, provided the factor is not too small. How small is determined empirically and is about 0.2 for the $\times 3'$ configuration and about 0.06 in the $\times 2'$.

The global distributions of A_{MH} and B_{MH} from (13) and (18), subject to (19), for the $\times 2'$ configuration near the surface are shown in Figs. 1a and 1b, respectively. Low, physical values of B_{MH} occupy most of the equatorial Pacific, but less than half of the Atlantic. Near the western boundaries with either land or bottom topography, B_{Munk} governs B_{MH} from the equator poleward to about 50°, where the decreasing Δx^3 in (15) first makes B_{Munk} smaller than the increasing B_{eddy} from (17). At western equatorial boundaries, the viscosity is most isotropic with $A_{MH} = 133 \times 10^3$ and $B_{MH} = 86 \times 10^3$ m^2 s^{-1}. According to (13), A_{MH} is largest at the surface along the equator where Δx and $V(z)$ are largest. The reduction in both coefficients due to (19) occurs only poleward of about 83°N. Everywhere above about 1000-m depth, the dissipation is nonnegative-definite, because A_{MH} is larger than B_{MH}. This is true all the way to the ocean bottom only in the Tropics and away from western boundaries.

3. The numerical experiments

The surface forcing is computed using the bulk scheme described in Large et al. (1997). In nonpolar seas, the inputs are the near-surface atmospheric state (winds, temperature, density, and humidity), net solar flux, cloud coverage, and precipitation. The evolving model SST and bulk formulae are then used to give the surface fluxes of momentum, heat, and freshwater. All inputs are on a nominal 2° grid, then interpolated to the model tracer points. A further interpolation to the velocity points allows the wind stress to be applied as boundary conditions for F_V^u and F_V^v of (1). The Arakawa B grid has velocity points at the equator, so the nearest tracer points are at $\pm\Delta\phi/2$.

Unfortunately, no set of forcing data is entirely satisfactory. Since equatorial circulation is most sensitive to the winds, an attractive choice is to use the annual cycle (August 1996–July 1997) of 6-hourly satellite scatterometer-based global winds (SCAT) constructed by Milliff et al. (1999). In equatorial regions they find these winds to be superior to those from the National Centers for Environmental Prediction (NCEP) reanalysis (Kalnay et al. 1996). Grima et al. (1999) report more realistic equatorial current variability with scatterometer wind forcing than with winds from an atmospheric model. Nonetheless, the atmospheric state is always completed with 6-hourly NCEP air temperature and humidity (August 1996–July 1997). Other forcing data are monthly precipitation over this period (Xie and Arkin 1996) and the monthly climatological (1983–91) annual cycles from International Satellite Cloud Climatology Project solar radiation (Bishop and Rossow 1991) and cloud cover (Rossow and Schiffer 1991).

Vertical mixing coefficients are variable because they depend on the evolving ocean state, on the wind, as characterized by the friction velocity u^*, and on the surface buoyancy flux into the ocean, B_o. They are determined from the KPP scheme developed by Large et al. (1994) and validated at the equator by Large and Gent (1999):

$$A_{MV} = \begin{cases} u^* h H\left(\dfrac{-z}{h}, \dfrac{zB_o}{u^{*3}}\right), & -z \le h \\ \nu_m^w + \nu^s(\text{Ri}_g), & -z \ge h, \end{cases} \tag{20}$$

where h is a diagnosed boundary layer depth, and Ri_g is the local gradient Richardson number. The dimensionless function H makes A_{MV} and its first vertical derivative continuous at $-z = h$, and $A_{MV} = 0$ at the surface. Below h, vertical mixing is similar overall to some implementations of the Pacanowski and Philander (1981) parameterization. It is regarded as the superpo-

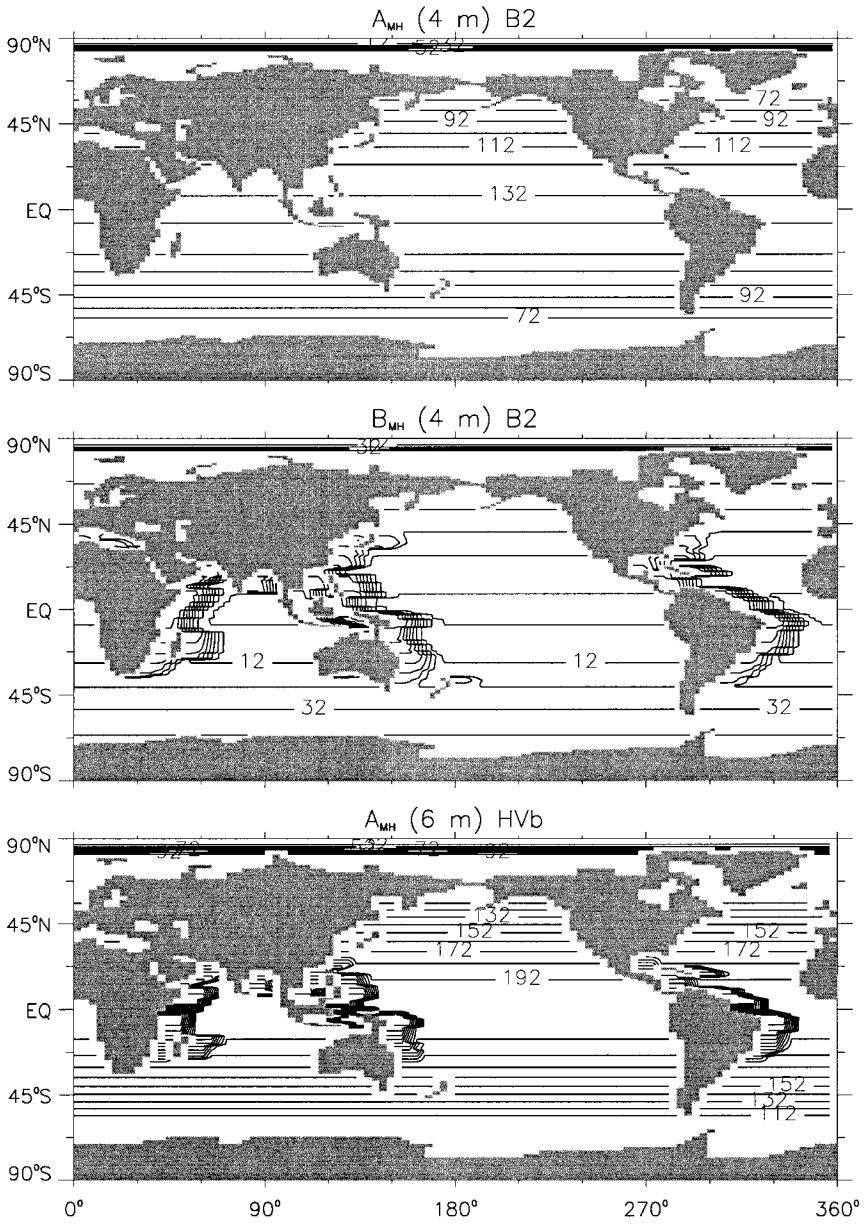

FIG. 1. The anisotropic viscosity coefficients A_{MH} and B_{MH} at 4-m depth for the global $\times 2'$ base case (B2), and the isotropic viscosity coefficient for the global $\times 3'$ case HVb. Units are 1000 $m^2\ s^{-1}$ and the contour interval is 10 units.

sition of two downgradient diffusion processes; internal wave breaking with a constant viscosity coefficient, ν_m^w, and shear instability. The viscosity of the latter process, ν^s, is positive for $Ri_g < 0.8$ and a maximum of 50 $cm^2\ s^{-1}$ at $Ri_g = 0$.

The design of the numerical integrations recognizes the rapid response of the equatorial ocean, as well as the nearly 10 times greater computational demands of the $\times 2'$ model over the $\times 3'$. Base case solutions for both B2 and B3, respectively, were obtained. Starting from rest, but with equilibrated temperature and salinity from a past long integration with isotropic, but spatially varying horizontal viscosity, the B3 case was forced by 10 repeating annual cycles of SCAT forcing. The B3 solution after 5 years was interpolated as initial conditions for the B2 case, which ended after 5 more years of SCAT forcing.

Table 1 lists the relevant model parameters for these two base cases and the changes made for all subsequent $\times 3'$ experiments. Two repeats of B3 were designed to show how the anisotropic viscosity formulation of section 2 improved equatorial currents. The first, HVa, used the constant viscosity of Large et al. (1997); $A_{MH} = B_{MH} = 300 \times 10^3\ m^2\ s^{-1}$. The second, HVb, used isotropic

TABLE 1. Model parameters for the two base cases, B2 and B3, and all the ×3′ sensitivity experiments. A blank entry indicates no change from B3.

Case	Winds	Viscosity V_m^w ($cm^2\ s^{-1}$)	Viscosity A_{MH} ($m^2\ s^{-1}$)	Viscosity B_{MH} ($m^2\ s^{-1}$)
B2	SCAT	1	(13)	(18)
B3	SCAT	1	(13)	(18)
HVa			300 000	
HVb			MAX (A_{MH}, B_{MH})	
NCEP	NCEP			
V.5		0.5		
V16.7		16.7		

viscosity equal to the maximum of A_{MH} and B_{MH}, and its near-surface distribution is shown in Fig. 1c. This viscosity is governed by large values of B_{MH} only within about 20° longitude of tropical and subtropical western boundaries. Another repeat of B3 (NCEP) used NCEP wind forcing from August 1996 through July 1997, in order to further quantify the effects of the different winds. Finally, the sensitivity to one part of the vertical viscosity (20) was investigated with two repeats of B3; V.5 and V16.7 with ν_m^w set to 0.5 $cm^2\ s^{-1}$ and to the 16.7 $cm^2\ s^{-1}$ value of Large et al. (1997), respectively.

4. Comparisons with observations

The better base case result ought to be B2. It has lower mixing coefficients by virtue of its finer resolution, and nonnegative-definite dissipation throughout the region of interest (see Fig. 1). Its mean zonal currents along the equatorial Pacific (Fig. 2a) are indeed comparable to the climatological annual mean (Fig. 2b) and the August 1996 through July 1997 mean (Fig. 2c) from TAO current meter records. The respective maximum eastward undercurrent velocities, $U_{\rm EUC}$, are 95.4, 96.4, and 101 cm s^{-1}. The improvement over previous model implementations with $U_{\rm EUC} < 15$ cm s^{-1} is dramatic. Also well represented are the rise in the core of the EUC from a depth about 200 m in the west to about 70 m in the east, and the predominantly westward flow near the surface.

More aspects of the B2 solution will now be compared to observations in the Pacific and, less extensively, in the equatorial Atlantic and Indian Oceans. This exercise leads to the following conclusions regarding differences found in these comparisons and in Fig. 2. In the Pacific, the model compares more favorably with spatially averaged drifter data than point current meter observations (section 4a). The repeat wind forcing, the monthly precipitation, and the climatological radiation are responsible for differences in the monthly mean zonal velocity (section 4b) and hence annual means (Fig. 2). General circulation deficiencies (section 4c) may be causing problems with modeled currents and water masses north of the equator. With the B2 configuration, specifying the horizontal viscosity in the Atlantic remains problematic (section 4d). Finally, interannual variability could explain differences in the zonal velocity of the Indian Ocean (section 4e).

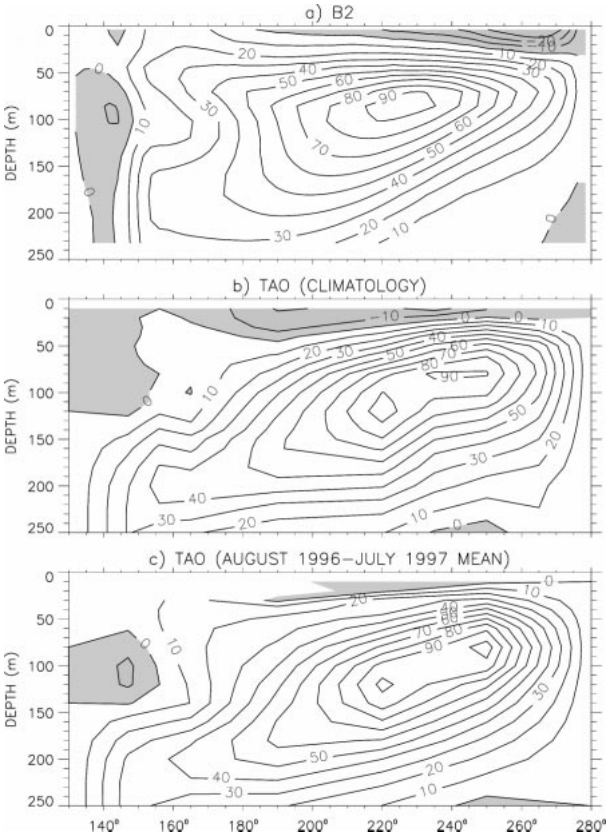

FIG. 2. Zonal sections across the Pacific of zonal velocity at the equator: (a) annual average of case B2, (b) TAO current meter climatological annual mean, (c) TAO current meter 1-yr mean, Aug 1996–Jul 1997. Contour interval is 10 cm s^{-1} and westward flow regions are shaded.

a. Climatological $u(\lambda, \phi)$ and $v(\lambda, \phi)$ from near-surface drifters

The extensive drifter observations in the equatorial Pacific provide the most complete observations of the horizontal structure of equatorial currents, but horizontal averaging over very large bins (2° lat by 12° long) is required because of the sampling. The drogue depth extends between about 10- and 20-m, so the drifter velocities are reported at $z = -15$ m. The most compatible model velocity is a weighted average of the second level, which spans the depth range 8–17 m and the third level (17–27 m). Figure 3 shows that the modeled and observed $u(\lambda, \phi, -15\ \text{m})$ in the Pacific have similar features. The eastward flowing North Equatorial Countercurrent (NECC) is evident between 4° and 8°N. Although its modeled strength is much stronger than in previous configurations, it is only about one-half that observed across the basin, though the spatial patterns

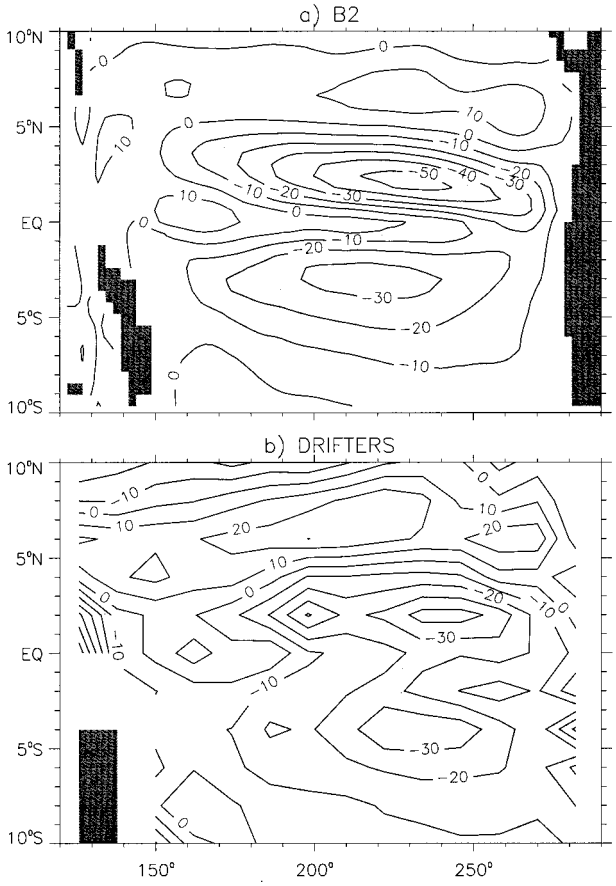

FIG. 3. Zonal velocity at 15-m depth as a function of latitude and longitude: (a) annual average of case B2, (b) climatology of equatorial drifter deployments averaged over 2° lat by 12° long bins. Contour interval is 10 cm s^{-1}, and westward flow regions are shaded.

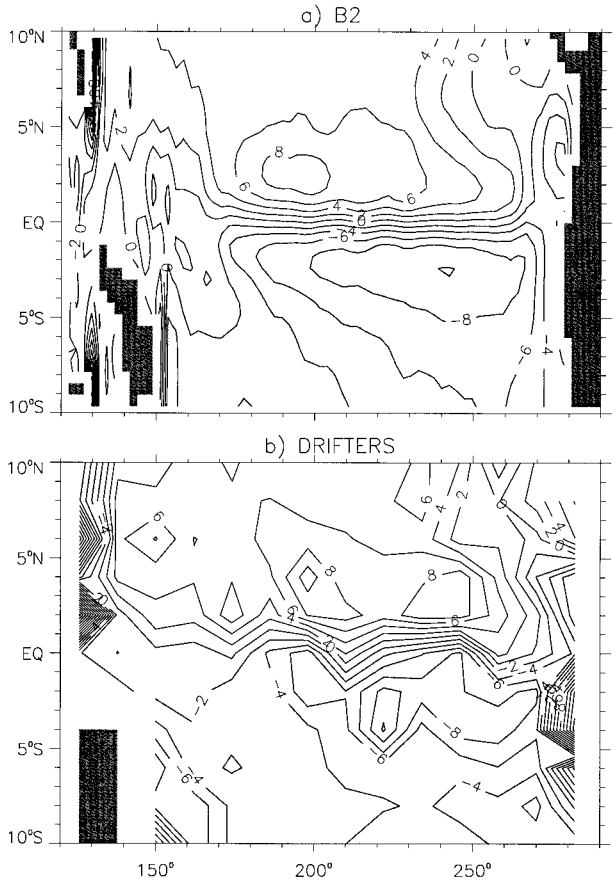

FIG. 4. As in Fig. 3 except for meridional velocity with a contour interval of 2 cm s^{-1}, and southward flow regions shaded.

are strikingly similar. Both the model and drifters show a maximum in westward flow at about 3°S and between 1.5° and 3.5°N, where it is stronger. In between lies the equator where the model has a sharper feature and more eastward flow than the drifter data, perhaps due in part to the large meridional averaging of the latter. In the model this feature is caused by the eastward flowing EUC below.

Analysis of the zonal momentum budget reveals that this influence is exerted in two ways. First, there is a turbulent drag characterized by negative momentum flux ($\sigma_{13} < 0$) all the way from the EUC core to the surface, such that the F_V^u term of (1a) and (9) is also negative throughout these depths. Thus, this term scales with the zonal surface stress divided by the depth of the EUC. Without an EUC, its magnitude would be greater by more than a factor of 2, because it would scale with the shallower depth (typically less than 50 m) of the boundary layer, where the surface heat and freshwater fluxes are found. Second, there is the upwelling of more eastward flowing deeper water. In particular, the vertical advection [wu_z part of the $(wu)_z$ term of (2)] is not negligible compared to the zonal pressure gradient in balancing F_V^u in (1a). Furthermore, this feature is not diffused meridionally because F_H^u remains only about 10% of these terms. Without the small value of B_{MH} in (7), away from western boundaries (Fig. 1), this viscous term would dominate and the role of advection would diminish.

Drifter and model meridional velocities at $z = -15$ m are compared in Fig. 4. They both show similar equatorial divergence: southward flow at 8–10 cm s^{-1} at about 2°S, and northward flow at 8–10 cm s^{-1} at about 3°N. Along much of the equator the average meridional velocity is near zero in both the model and drifters, but the latter display more variability. Off the coast of South America, the drifters show strong equatorward flow in both hemispheres, but the model has northward flow in the Southern Hemisphere only in its 8-m-thick uppermost level.

Prognostic model velocities represent the flow over a three-dimensional model grid cell. Therefore, they are not directly comparable to current meter observations from a point in space; especially in the highly sheared flows of the equatorial oceans. On the other hand, trajectories of surface drifters whose drogues span the

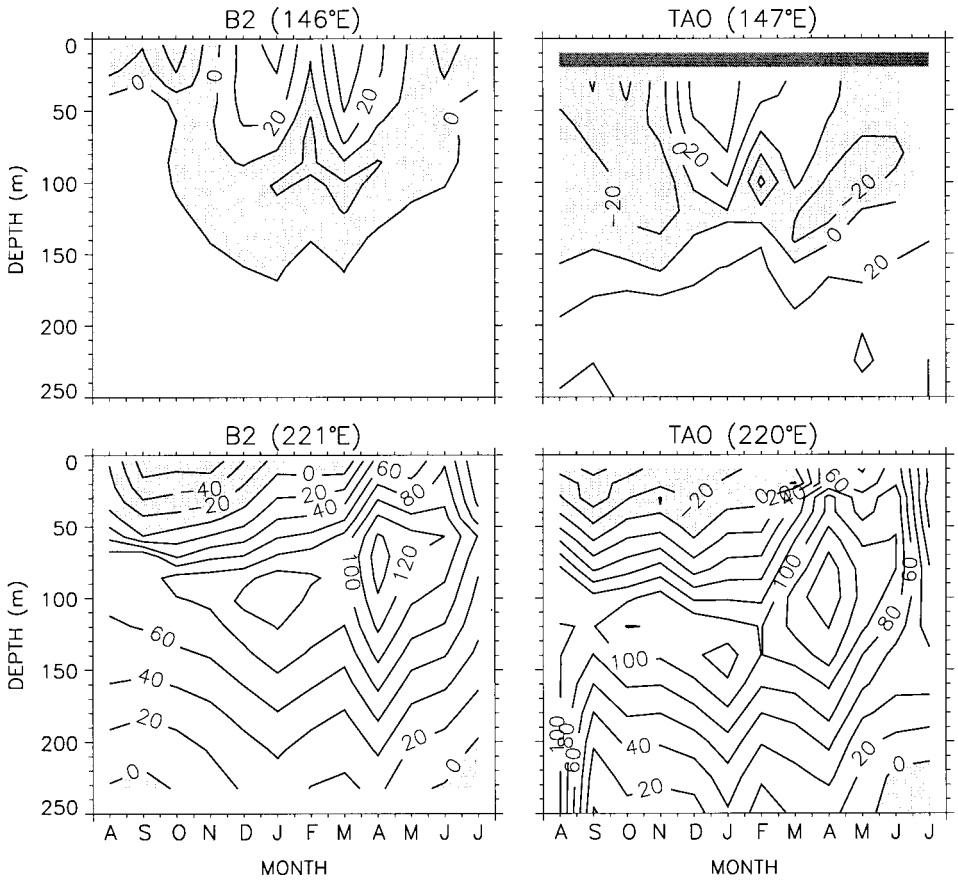

FIG. 5. One year cycle, starting with Aug 1996, of monthly mean zonal velocity at the equator as a function of depth from case B2 and from the TAO current meters. The two locations are (top) 147°E and (bottom) 220°E. The contour interval is 20 cm s^{-1}, and westward flow regions are shaded.

depths of a model grid level potentially could provide more compatible velocities. Although the drifter observations fall short of this ideal, we indeed find that in some ways the model (Figs. 2a and 3a) agrees better at the equator with the spatially averaged drifter data (Fig. 3b) than the point current meter climatology (Fig. 2b). For example, the three respective values for $u(0°, 160°E, -15$ m) are about 15, 15, and 0 cm s^{-1} and for $u(0°, 260°E, -15$ m) they are about -22, -24, and -5 cm s^{-1}.

b. Annual cycle of zonal velocity profiles

Twelve monthly means (August 1996–July 1997) of zonal velocity from current meters and the model are shown in Fig. 5. This comparison is complicated by the strong 1997 ENSO warm event, and this problem may explain some of the differences in Fig. 2. The repeat annual cycle of winds is necessary to spin up the model currents and evolve the temperature and salinity away from their initial conditions. There is a smooth transition of the atmospheric state forcing over the last 5 days of July 1997 and the first 5 days of August 1996, but there is no attempt to initialize the model with velocity, temperature, and salinity fields appropriate for August 1996 because the observations are incomplete. Instead, the ocean state at the beginning of each August 1996 is representative of July 1997 conditions, and a much poorer initial condition than would have been the case if 1997 had been a more normal year.

Where the observed and modeled currents are similar in August, they tend to remain so throughout the year and, therefore, the annual means (Fig. 2) compare well. An example is at 220°E, above about 70 m (Fig. 5, lower panels). Deeper, such is not the case. In August 1996, the current meters below 150 m show a very strong uniform eastward flow at 100 cm s^{-1} that remains stronger than the model throughout the year. As a result, the model annual mean currents (Fig. 2a) are 10–20 cm s^{-1} smaller at these depths than in Fig. 2c. It would appear that this problem is also at least partially responsible for the shallower and weaker maximum at 220°E in Fig. 2a, compared to Fig. 2b and Fig. 2c. However, the observed evolution of the EUC at 220°E (its rise from March to June, maximum of more than 140 cm s^{-1} in

April, and disappearance in July) is reproduced by the model.

The model August conditions are also quite different than observed at 147°E (Fig. 5, top panels). Although neither the model, nor the current meters display much monthly variability below 150 m, the latter display more vertical shear in August and throughout the year. Therefore, the annual means differ, with Fig. 2a displaying much less shear between 150 and 200 m depth. Instead the corresponding shear appears to develop about 10° farther east. Above 150-m depth, the model reproduces much of the observed pattern of westward flow. The initial westward flow is interrupted by two westerly wind bursts that force eastward flow with peaks in January and March. The modeled and observed responses to the first are similar both in magnitude and depth of penetration. However, in March the modeled currents at depth are stronger eastward, perhaps because the monthly precipitation, or the climatological radiation allows the response to penetrate too deep. Between 150° and 170°E, the model (Fig. 2a) has a maximum u between 40 and 70 m depth that is not evident in the climatology (Fig. 2b). Although weaker, such a feature is seen by the current meters from August 1996 to July 1997 (Fig. 2c). This result suggests that the currents west of the date line and above 100 m are very dependent on the response to westerly wind bursts, and that all model forcing, not just the winds, should resolve the diurnal cycle, and be concurrent with the timeframe of the observations being compared.

c. Meridional sections of climatological temperature and salinity

Baroclinic pressure gradients are important terms in the momentum equations (1) and couple the equatorial currents to the ocean's potential temperature, θ, and salinity, S. Climatological sections of θ and S from 10°S to 10°N along 165°E, 205°E, and 250°E are shown in Johnson and Moore (1997; Fig. 1). These sections show that the Levitus and Boyer (1994) and Levitus et al. (1994) climatologies overly smooth the meridional structures near the equator. Since these structures are present in the model, they are now compared with Johnson and Moore (1997). It appears that the model's general circulation could be improved to produce more realistic water masses north of the equator and at depth.

To illustrate, corresponding sections from case B2 are shown in Fig. 6. South of the equator, the model and observed water masses are much the same. The salinity maxima are at the same depth, have similar temperature and salinity, the same variation with longitude, and penetrate to about the same latitude. This penetration is terminated by a salinity front. This front is too strong in the model at 205°E because of a tongue of too fresh water coming from the north between about 80 and 250 m. Otherwise the model salinities north of the equator are comparable to the climatological sections. However, from 6° to 10°N the observed meridional temperature gradient is systematically stronger than the model, which is related to the model's weak NECC. The depth of the 20°C isotherm is generally in good agreement between model and observed sections, but deeper the model has a warm bias, with some density compensation provided by overall saltier water.

d. Zonal velocity in the Atlantic Ocean

The anisotropic viscosity formulation of section 2 is less successful in the Atlantic, though a big improvement over previous implementations. The annual mean zonal velocity from the modeled Atlantic (Fig. 7a) does not compare very well with the current meter records of Weisberg and Colin (1986). In these observations the core of the EUC at 28°W varies from about 60 to 100 cm s^{-1} eastward, while the Fig. 7a value is less than 35 cm s^{-1}. By chance, this location is near 25°W where (15, 16, 17, and 18) give $B_{MH} = B_{\text{Munk}} = B_{\text{eddy}} = A_{\text{eddy}}$ (Fig. 1). It appears as if the rapidly increasing viscosity to the west (upstream) causes the EUC strength to be weak downstream even where the viscosity is more physical. This is also the case farther east at 4°W where the current meters report core EUC speeds between about 50 and 80 cm s^{-1}, but the model value is still low at only about 25 cm s^{-1}. It is interesting that the depth of the model's Atlantic EUC does agree with the observed behavior. It has a distinct annual cycle at 4°W that is shallowest in late April at about 65 m, deepening to 100 m by early October. At 25°W the annual cycle is much reduced and the mean depth is only about 60 m. Because it is weaker, the EUC does not exert sufficient influence near the surface where the flow, therefore, is more westward than observed at both current meter locations. The zonal momentum budget (1a) indicates that the role of turbulent drag is similar to the Pacific (section 4a), but vertical advection is weaker.

e. Zonal velocity in the Indian Ocean

The annual mean zonal velocity across the modeled equatorial Indian Ocean is shown in Fig. 7b, but the problem of finding contemporaneous forcing and ocean observations is particularly acute in this basin. Current meter records from the Indian Ocean are dominated by semiannual period variability in response to the semiannual fluctuations in the zonal wind stress (Luyten and Roemmich 1982; McPhaden 1982). In accord is Fig. 8, which shows the annual cycle of zonal wind stress and model velocity at (0.6°S, 72°E). The location and vertical averaging are chosen to match McPhaden (1982, Fig. 1). Both wind records show zonal stress approaching 0.05 N m^{-2} in May and October, with corresponding maxima in the 0–17-m average current reaching nearly 100 cm s^{-1}. Westward wind stress tends to occur in two periods, January–March and June–August, and in response the flow reverses; in phase at the surface, and

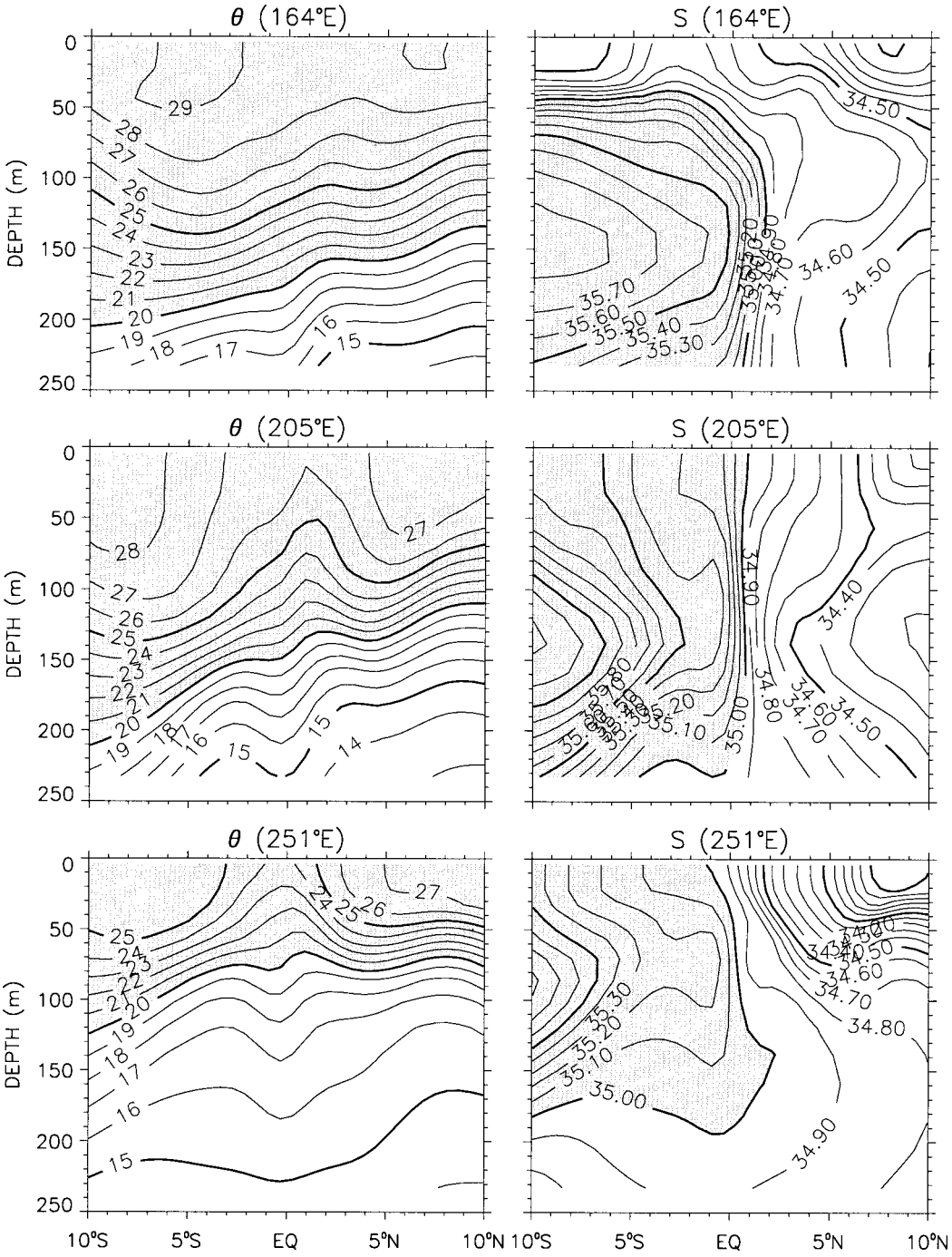

FIG. 6. Meridional sections from 10°S to 10°N of potential temperature, θ, and salinity, S, from case B2. The locations near (top) 165°E, (middle) 205°E, and (bottom) 250°E were chosen to match Johnson and Moore (1997, Fig. 1), as are the contour intervals of 1°C and 0.1 psu.

out-of-phase at depth (Fig. 8c). Such westward stress appears to have been more common in the year August 1996 to July 1997 than between January 1973 and May 1975 so that the model has stronger near-surface westward flow ($u < -50$ cm s^{-1} for 4 of 12 months, Fig. 8b) than the observations ($u < -50$ cm s^{-1} for 1 of 29 months). This interannual variability is likely a major source of the weaker mean eastward flow in the upper 200 m of Fig. 7b at 72°E than shown in McPhaden (1982, Fig. 3). Deeper, between 160 and 180 m, the model currents compare most favorably with the last year of the observed record, where the monthly mean

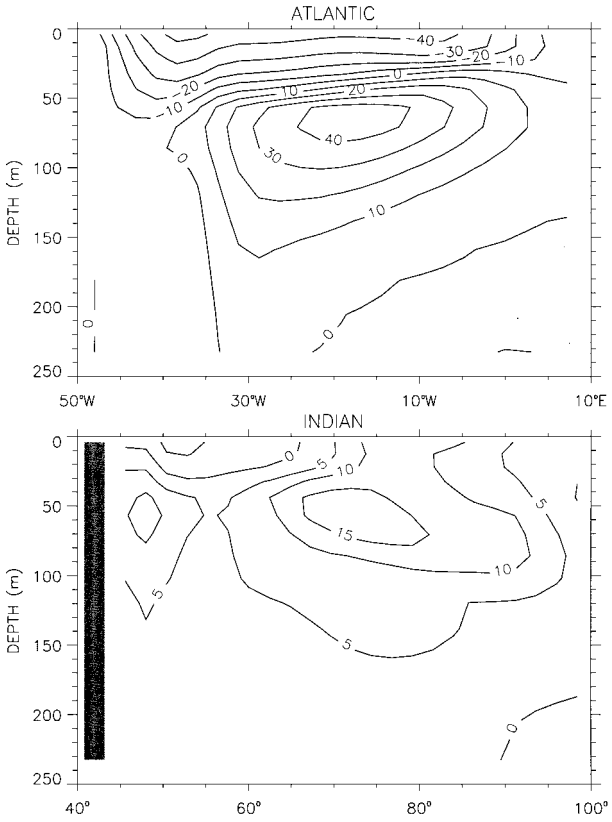

FIG. 7. Zonal sections across the Atlantic and Indian Oceans of annual mean zonal velocity at the equator from case B2. Contour interval is 10 cm s^{-1} in the Atlantic and 5 cm s^{-1} in the Indian, and westward flow regions are shaded.

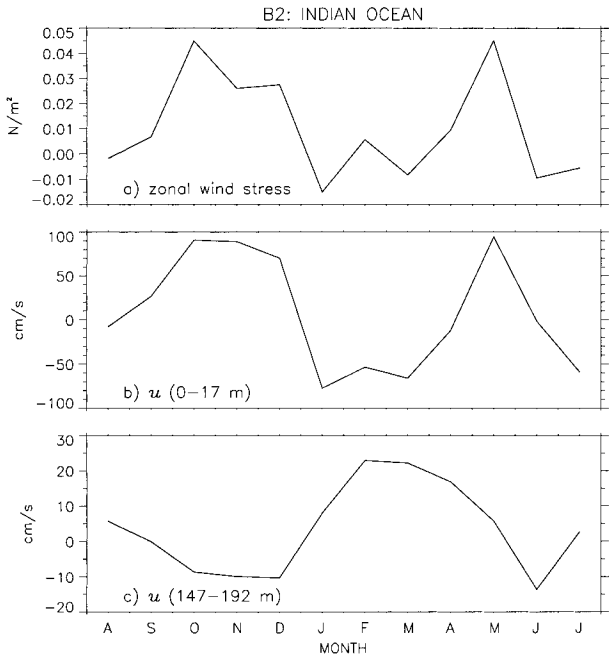

FIG. 8. One year cycle of monthly means from case B2 starting with Aug 1996 of (a) zonal wind stress, and zonal current averaged over depth (b) 0–17-m, and (c) 147–192-m. The location (72°E, 0.6°S) and depth intervals were chosen to match McPhaden (1982, Fig. 1) closely.

zonal current varies from −1 to 20 cm s^{-1}. The variability of the corresponding model flow in Fig. 8c, like the near-surface currents (Fig. 8b), is comparable to these observations, so the viscosity does not appear to be too large in this region of the Indian Ocean.

5. Model sensitivities

Sensitivity experiments (Table 1) are performed using the less computationally demanding ×3′ configuration. An advantage of the anisotropic viscosity formulation of section 2 is that it explicitly includes how the horizontal viscosity should vary with resolution. The sensitivities in the ×3′ should be valid for the ×2′ because the B2 and B3 solutions are very similar with regard to equatorial currents. Thus, the larger area of $A_{MH} < B_{MH}$ in B3 does not appear to be a serious problem. The meridional sections along 220°E in Fig. 9 provide an illustration of this similarity, as well as the meridional structure of the model solutions. In both, the eastward flow of the EUC extends from about 15 to 250 m, the core depth is between 90 and 100 m, with a speed between 90 and 95 cm s^{-1}. Also both sections show an asymmetric South Equatorial Current that is stronger westward to the north and has a minimum right at the equator where the force exerted by the EUC is maximum (section 4a). Except for the weak NECC evident at both resolutions, the model features are very much like the Hawaii to Tahiti shuttle results of Wyrtki and Kilonsky (1984) and the drifter observations (Figs. 3 and 4).

A useful diagnostic of overall model sensitivity, especially with regard to the climatically important SST, is upwelling. Meridional sections from three cases are shown in Fig. 10, where the vertical velocity is an annual mean, averaged between 180° and 260°E in the Pacific. The expected upwelling on the equator and downwelling poleward is evident in every case. The strength is about 10% stronger in B2 (not shown) than in B3 (Fig. 10a): 19.8 versus 17.7 ($\times 10^{-6}$ m s^{-1}) for the maximum upwelling and −3.3 versus −2.9 ($\times 10^{-6}$ m s^{-1}) for the maximum downwelling. For comparison, the diagnostic model of Bryden and Brady (1985) gives a somewhat larger equatorial upwelling with a maximum of 29 × 10^{-6} m s^{-1} at about the same depth (50–60 m). They also find a much stronger downwelling below 180 m. Their model uses geostrophy to compute a stronger EUC ($U_{\rm EUC} > 120$ cm s^{-1}), which may cause some of the difference in vertical velocity.

a. Anisotropic versus isotropic viscosity

Compared to B3, cases HVa and HVb differ only in their formulation of horizontal viscosity. In HVa it is

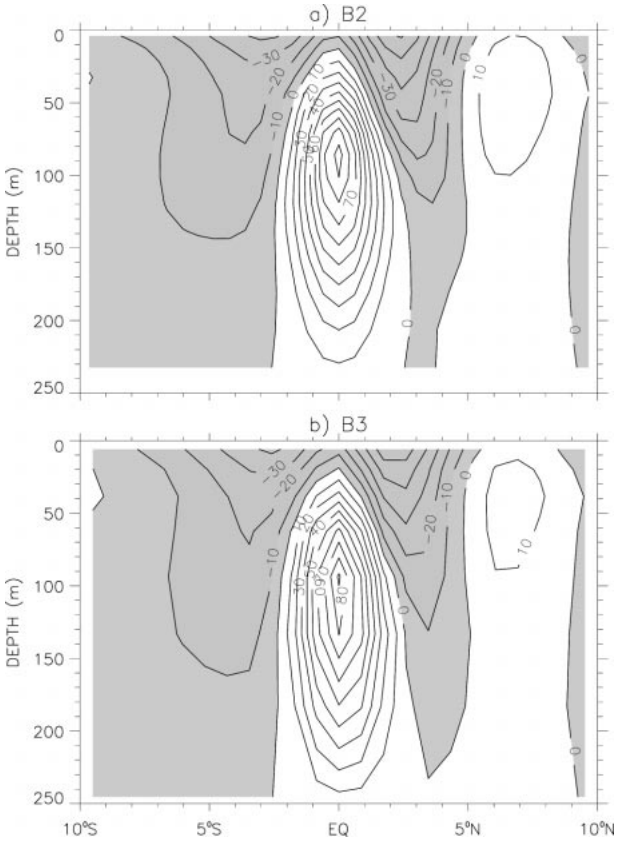

FIG. 9. Meridional sections from 10°S to 10°N of annual mean zonal velocity near 220°E from (a) case B2 and (b) case B3. Contour level is 10 cm s^{-1}, and westward flow regions are shaded.

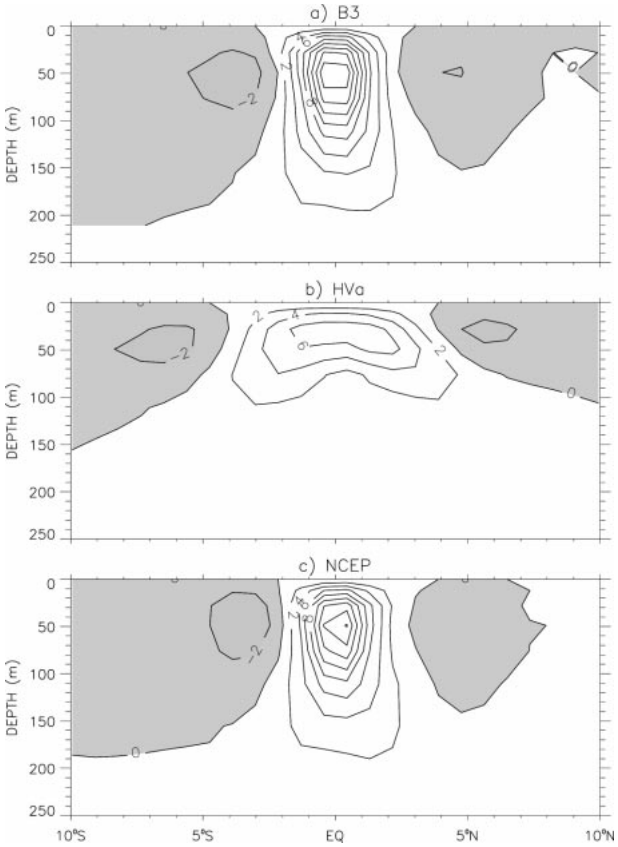

FIG. 10. Meridional sections from 10°S to 10°N of annual mean vertical velocity, averaged from 180° to 260°E from (a) case B3, (b) case HVa, and (c) case NCEP. The contour interval is 2×10^{-6} m s^{-1}, and downwelling regions are shaded.

constant and identical to Large et al. (1997) and similarly weak equatorial currents result. Compared to B3 (Fig. 10a), the much weaker and broader upwelling between 4°S and 4°N, is shown in Fig. 10b. The upwelling is also shallower, which would tend to bring up warmer water and maintain a warmer SST. Off the equator the downwelling in case HVa is as strong, or even stronger than B3, but shallower and displaced poleward. For the model resolutions considered here, allowing an isotropic viscosity coefficient to be spatially variable is not very effective at strengthening equatorial circulation. To illustrate, Fig. 11 shows that the meridional sections of zonal velocity from HVa and HVb are very similar. There are broad, weak EUCs with deep cores at about 130 m. Near the surface both solutions are very different from the drifter observations. The maximum westward speeds are right on the equator, not only at 220°E (Fig. 11) but across the whole Pacific. Between 5° and 9°N the NECC is very poorly represented by very weak eastward flows at depth. In contrast to the observations, the near-surface currents are westward at these latitudes too. Off the equator the poleward velocities are much too weak compared to Fig. 4.

In contrast, anisotropy is very effective in bringing equatorial current speeds and shears up to realistic values. In the Pacific U_{EUC} is increased by nearly an order of magnitude in B3 (Fig. 9b) compared to HVa and HVb (Fig. 11), and the NECC is much improved. As shown in section 4, other aspects of the equatorial current systems also become more like observations. However, the price for this improvement is a greater propensity for numerical noise, as shown by the zonal sections of meridional velocity in Fig. 12. Two contour intervals in these sections are set at ± 0.05 cm s^{-1}; an arbitrary level of acceptable noise. A design criterion has been to not have either the plus or minus 0.05 cm s^{-1} contour appear in any noise pattern on the grid scale. Between 400 m and the bottom, where the velocities become small, both base cases (Fig. 12a and Fig. 12b) display such noise, but the amplitude criterion is satisfied except for a small area at about 400-m depth in both B2 and B3. Vertically coherent regions of northward flow are separated by $2\Delta\lambda$: 4.8° in B2 and 7.2° in B3. This type of noise appears to emanate from western boundaries and can be suppressed by reducing the effect of the function, $p(x)$ in (15); the rate at which B_{Munk} decreases away from western boundaries. This can be accomplished by either increasing L_M or making N larger in (16), but at the cost of reducing the Pacific EUC below its observed strength.

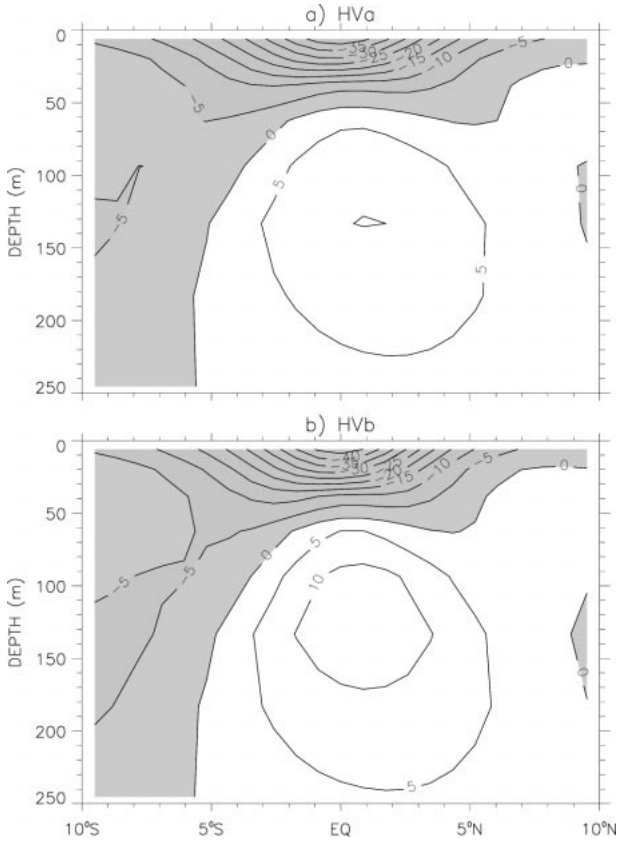

FIG. 11. Meridional sections from 10°S to 10°N of annual mean zonal velocity at 220°E from (a) case HVa and (b) case HVb. Contour interval is 10 cm s^{-1}, and westward flow regions are shaded.

This first type of noise is eliminated with the spatially variable, isotropic viscosity of HVb (Fig. 12d). However, the grid Reynolds number criterion (12) is not entirely satisfied in this case, though the resulting noise is at an acceptable level. The signature of this second type of noise is a horizontally coherent pattern with regions of positive and negative v two model layers apart in the vertical (Fig. 12d). It is superimposed on the first, vertical pattern in B3 (Fig. 12b), but is not so apparent in B2 (Fig. 12a). The constant high isotropic viscosity of HVa effectively eliminates both types of noise (Fig. 12c), but only at the expense of much of the realism in equatorial currents. Despite their small scales, the meridional velocity structures in the west are not numerical noise because they are evident in all solutions, including the viscous HVa.

b. Wind forcing

One of the apparent problems with NCEP wind forcing is that the westward wind stress along the equatorial Pacific is about 10% less compared to SCAT winds (Milliff et al. 1999). In general accord with the Cane and Sarachik (1977) analytic result, U_{EUC} from the NCEP case is only 83 cm s^{-1}, or 14% less than in B3. Grima et al. (1999, Fig. 4) show an even larger change (>20%) in their comparison of winds from a different atmospheric model and different scatterometer. Across the equatorial Atlantic and Indian Oceans, the differences between NCEP and SCAT zonal winds are neither as large nor as systematic. Therefore, the two wind forcings produce very much the same zonal currents in these basins.

Milliff et al. (1999) also show that there are systematic differences in the meridional wind stress in the equatorial Pacific and Atlantic Oceans. In general, this stress is the same in both datasets at about 6°S, where it is northward, and at about 13°N, where it is southward. However, the convergence occurs over all 19 degrees in the NCEP case, but is confined to a distinct ITCZ between 3°N and 10°N in the SCAT winds. The greater SCAT northward stress at the equator drives more cross-equator flow.

In order to demonstrate the overall effect of the different winds on equatorial upwelling, Fig. 10c also shows a meridional section of annual-mean vertical velocity from the NCEP case. The more convergent NCEP forcing at the equator locally contributes to reduced upwelling at all depths compared to B3 (Fig. 10a). The maximum is reduced by about 10%. A similarly diminished upwelling occurs in the Atlantic. Around 5°N the more convergent SCAT winds produce a larger downwelling, but between 3° and 4°S slightly larger downwelling results from the NCEP winds.

With stronger westward stress in the Pacific compared to NCEP, B3 might be expected to have stronger westward surface flow, but this is not the case. The zonal momentum budget (1a) shows that above about 100 m, the increase in the B3 pressure gradient only balances about one-half of the change in F^u_V. The bulk of the remainder is balanced by advection; in particular wu_z. Thus, the greater upwelling and stronger eastward flowing EUC of B3 combine to more than overcome the more westward zonal wind so that scatterometer winds produce weaker westward near-surface flow all across the Pacific. There are two other important factors in this scenario. First, the adjustments of the surface flow and EUC compensate to keep the overall shear between the surface and the EUC about the same in both cases. Therefore, the turbulent drag between the surface and EUC is always important, but almost unchanged between B3 and NCEP. Second, with $B_{MH} = A_{\mathrm{eddy}}$, the F^u_H term of (1a) remains small in both B3 and NCEP, which allows changes in other terms (e.g., vertical advection) to influence the flow field.

c. Internal wave mixing

The vertical viscosity ν^w_m in (20) governs only mixing due to internal waves. In the surface boundary layer it is not involved directly in the mixing. Nonetheless, equatorial currents are dependent on this parameter because it governs vertical turbulent momentum transfer

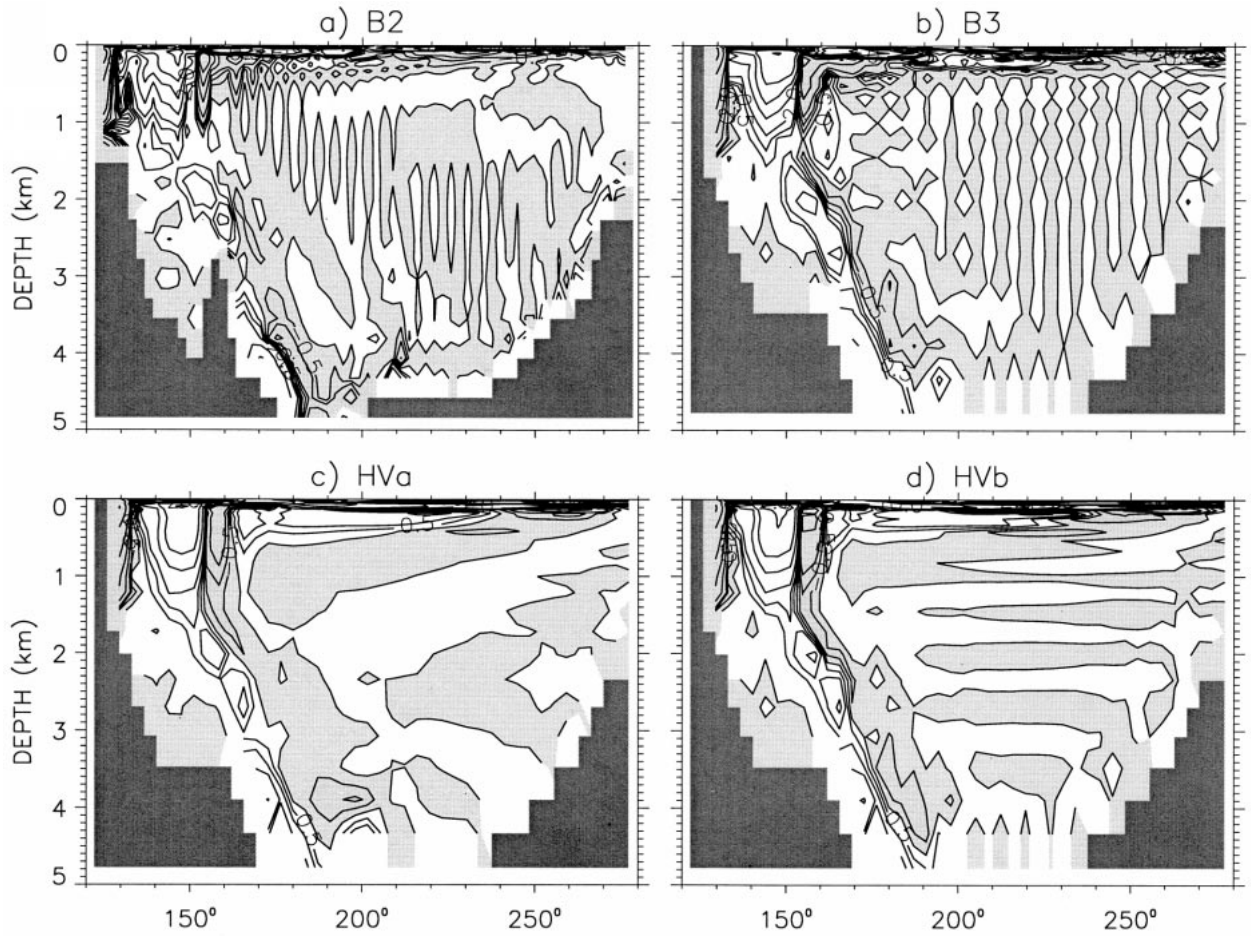

FIG. 12. Zonal section of annual mean meridional velocity along the equatorial Pacific from (a) case B2, (b) case B3, (c) case HVa, and (d) case HVb. Contours are irregular at 0, ±0.5, ±1, ±2, ±5, ±10, ±20, ±50, ±100, and ±200 mm s^{-1}. The zero contour separates shaded southward flow from unshaded northward flow.

between the EUC core and deeper waters and it combines with shear instability mixing between the core and the boundary layer. The overall sensitivity of the model to ν_m^w is found to differ between the Pacific and Atlantic because horizontal viscosity plays too prominent a role in the latter. This behavior is shown by comparing the three cases V.5, B3, and V16.7 (Table 1). The effects on the magnitude ($U_{\rm EUC}$), depth ($D_{\rm EUC}$), and longitude ($\lambda_{\rm EUC}$) of the maximum annual mean zonal velocity of the EUC are shown in Table 2. Also shown for both basins are the maximum westward surface velocity, U_o, and measures of the overall shear between $D_{\rm EUC}$ and the surface, $S_{\rm EQ}$ (in units of cm s^{-1} m^{-1}) and of the upwelling, $W_{\rm EQ}$.

With $\nu_m^w = 16.7$ cm^2 s^{-1}, the zonal momentum budget (1a) in both basins is primarily a simple balance between the pressure gradient and F_V^u from the surface to below $D_{\rm EUC}$. Below $D_{\rm EUC}$, where $F_V^u = \nu_m^w u_{zz}$, vertical mixing with the slow moving abyss is much more of a brake on the EUC than it should be. This momentum exchange becomes much less important and perhaps more realistic in B3 when this viscosity is reduced to $\nu_m^w = 1.0$ cm^2 s^{-1}. There is little change in the pressure gradient at any depth, which, with less friction, accelerates the EUC, whose maximum is found at shallower depths and farther east (Table 2). In V16.7 the low shear, $S_{\rm EQ}$, means that internal wave viscosity dominates mixing between the EUC and boundary layer (20). When this process is reduced in B3, the shear adjusts until shear instability mixing can make up the difference, along with increased advection. This occurs with $S_{\rm EQ} = 1.3$ in both basins (Table 2). The vertical advection increases because of the larger shear and the greater upwelling, $W_{\rm EQ}$. In the Pacific, $U_{\rm EUC}$ reaches observed speeds (Fig. 9b) with advection balancing the pressure gradient at depths around $D_{\rm EUC}$. The larger $U_{\rm EUC}$ provides more than enough shear, $S_{\rm EQ}$, and reduces the westward near-surface flow, U_o. In the Atlantic the pressure gradient in the vicinity of $D_{\rm EUC}$ is balanced incorrectly by meridional viscosity, primarily the second term on the right-hand side of (7), because the coefficient, B_{MH}, is unphysically large over too much of this basin. As a result,

TABLE 2. Sensitivity of the annual mean equatorial zonal current structure to vertical viscosity due to internal waves, ν_m^w, in both Pacific and Atlantic Oceans. The maximum eastward velocity in the EUC has a speed $U_{\rm EUC}$ and is located at depth $D_{\rm EUC}$, and longitude $\lambda_{\rm EUC}$. The maximum upwelling anywhere along the equator is $W_{\rm EQ}$, and the minimum surface velocity is U_o. A measure of the overall surface to EUC shear is $S_{\rm EQ} = (U_{\rm EUC} - U_o)/D_{\rm EUC}$.

		Pacific						Atlantic					
Case	ν_m^w (cm^2 s^{-1})	$U_{\rm EUC}$ (cm s^{-1})	$D_{\rm EUC}$ (m)	$\lambda_{\rm EUC}$ (°E)	U_o (cm s^{-1})	$S_{\rm EQ}$ (cm s^{-1} m^{-1})	$W_{\rm EQ}$ (μm s^{-1})	$U_{\rm EUC}$ (cm s^{-1})	$D_{\rm EUC}$ (m)	$\lambda_{\rm EUC}$ (°E)	U_o (cm s^{-1} m^{-1})	$S_{\rm EQ}$ (cm s^{-1} m^{-1})	$W_{\rm EQ}$ (μm s^{-1})
V.5	0.5	100	95	232	−34	1.41	20	46	64	348	−45	1.42	10
B3	1	97	95	232	−35	1.39	20	40	64	348	−45	1.33	10
V16.7	16.7	40	140	210	−45	.61	12	11	105	338	−34	.43	6

the EUC fails to reach observed speeds ($U_{\rm EUC}$ = 40 cm s^{-1}, Table 2) and the westward near-surface flow increases until $S_{\rm EQ}$ = 1.3.

In B3, $\nu_m^w u_{zz}$ is not an important term at the depth of the EUC. Therefore, the factor of 2 reduction of ν_m^w in case V.5 causes little change in the EUC of either basin. With a similar EUC, other aspects of the equatorial currents are not very different either (Table 2). This convergence of solutions to an equatorial current structure resembling reality means that any value of ν_m^w less than about 1.0 cm^2 s^{-1} could have been used for the base cases B2 and B3.

6. Discussion and conclusions

A coarse-resolution climate model can be configured to produce equatorial currents comparable to observations, provided that a certain amount of numerical noise is accepted. In the present model, the key element is the spatially variable, anisotropic horizontal viscosity. It allows the coefficient of meridional diffusion of zonal momentum, B_{MH}, to be a physically based small value everywhere except near western boundaries. The scheme formulated in section 2 includes dependencies on grid size, so parameter values need to be found at only one resolution. This tuning procedure is greatly simplified by taking the numerical constraints (11), (12), and (19) to be equalities and by restricting the application to equatorial oceans, where the EUC requires V_o = 100 cm s^{-1} in (14). Then, the only open question is how $B_{\rm Munk}$ (15) should decrease away from western boundaries. The empirical result, (16) with L_M = 1000 km and N = 3, is a compromise between equatorial current strength and smoothness on the grid scale.

In the central Pacific the ×3′ horizontal resolution of $\Delta\lambda = 3.6°$, $\Delta\phi = 0.9°$ (B3) is found to be adequate. The weak, diffuse zonal flows of previous implementations are reproduced in case HVa, with a constant, isotropic viscosity of 300 × 10^3 m^2 s^{-1}. There is very little improvement with the spatially varying isotropic viscosity of case HVb. On the other hand, the spatially varying anisotropic viscosity of B3 not only improves zonal current structure and strength on and off the equator, it has a profound effect on meridional flow and on equatorial upwelling. Perhaps most significantly, it produces upwelling much deeper where it involves colder water in the surface heat budget.

Only a combination of $B_{MH} = A_{\rm eddy}$, scatterometer wind forcing, and ν_m^w less than about 1 cm^2 s^{-1} is found to produce a central Pacific EUC of the observed strength. This result may also depend on other aspects of the vertical viscosity (20). With weaker westward wind stress, the value of $U_{\rm EUC}$ in a model Pacific driven by NCEP reanalysis winds is about 10% weaker. It is not clear what the near-surface current in the model should be because neither the point current meter measurements nor the drifter bins correspond to the extent of the model grids. Nevertheless, the zonal component

of the model is strongly influenced by turbulent drag and vertical advection from the EUC below. These effects, including weaker upwelling, led to the unexpected result that weaker NCEP westward winds produce stronger westward near-surface flow in the Pacific. A different model momentum balance may not show the same response.

A large value of $\nu_m^w = 16.7$ cm^2 s^{-1} (V16.7) completely alters the momentum budget at the depths of the EUC because of the excessive downward momentum flux. The divergence of this flux, F_V^u, deepens and slows the EUC and becomes the primary balance of the pressure gradient. Once F_V^u ceases to be important, at $\nu_m^w = 1.0$ cm^2 s^{-1} (B3), there is little sensitivity to further reductions of ν_m^w (e.g., V.5). The sensitivity of the near-surface westward flow to reducing ν_m^w depends on how the pressure gradient becomes balanced in and below the EUC. In the Pacific it is the advection terms, that allow the EUC to reach observed speeds and reduce the westward surface flow. In the Atlantic this balance comes from an excessive meridional viscosity that makes the EUC too slow, with the net result that the surface flow becomes stronger westward. A very different sensitivity might be found in the Philander and Pacanowski (1984) model because the pressure gradient is not an important term below the thermocline (Wacongne 1989).

The finest horizontal resolution implemented ($\times 2'$) has $\Delta\lambda = 2.4°$, $\Delta\phi = 0.6°$ at the equator. Annual means from this case (B2) compare favorably with the extensive observations from the equatorial Pacific. Further comparison would require a model simulation including comprehensive initial conditions, complete and accurate forcing, and contemporaneous observations. In particular, it would be important to avoid problems associated with the large interannual variability in this region, such as the strong 1997 ENSO. Despite this event, the results do suggest that the ocean response to westerly wind bursts is an important factor in determining the vertical structure of annual mean zonal currents in the western tropical Pacific. The model is capable of a strong response to such events (e.g., December 1996), but precipitation and radiation forcing, at least daily, may be necessary for the proper modulation (e.g., March 1997). The model's large-scale general circulation in the Pacific produces more realistic water masses south of the equator. To the north the water is too fresh and there are weak meridional temperature gradients associated with a weak NECC.

The observational evidence from 72°E indicates that equatorial Indian Ocean currents are not overly attenuated in B2. The maximum monthly mean EUC speed of nearly 100 cm s^{-1} is comparable to the observations. Annual mean differences with limited current meter records can be attributed to interannual variability, at least until more extensive observations become available.

In the much narrower Atlantic equatorial basin it appears as if the viscosity, B_{MH}, remains too large too far east of South America, even in the $\times 2'$. One consequence is that the EUC never achieves an eastward velocity more than about half of that observed. Some improvement may be possible by reducing L_M and/or N in (16), but the noise penalty would be high for a modest gain. Figure 7 shows the EUC forming at about 35°W. If it is assumed that it will be sufficient to have $B_{MH} = A_{\text{eddy}}$ everywhere downstream of this point, then the required model resolution is about $\Delta\lambda = 1°$. Another aspect that may improve with finer zonal resolution is the depth of the equatorward surface flow off the coast of South America.

We view the formulation presented in section 2 for spatially variable, anisotropic eddy viscosities as provisional, so we have not been concerned with having $A_{MH} < B_{MH}$ away from our present regions of focus. With it we have achieved more satisfactorily strong and narrow equatorial currents in a coarse-resolution ocean model than with simpler formulations. Only at very fine resolution ($\Delta\lambda = \Delta\phi = 0.1°$) does the viscosity become nearly isotropic with a coefficient close to A_{eddy}, subject to (19). Such resolutions have only been configured for regional domains (e.g., Smith et al. 2000) and are not practical for global climate applications. Anisotropic horizontal eddy viscosity is a practical alternative, although $\Delta\lambda = 2.4°$ would appear to be too coarse in the Atlantic. We believe there may be further benefits with adaptive prescriptions for the coefficients, that is, functionals of the solution fields as well as the grid structure.

Acknowledgments. We wish to acknowledge the many individuals responsible for acquiring the equatorial ocean observations used in this study. In particular, the TOGA TAO Project Office, Dr. M. J. McPhaden, Director, made the TOGA TAO data freely and easily accessible, and Dr. P. P. Niiler generously provided processed surface drifter velocities. Dr. Rick Smith provided helpful insights into general viscosity formulations. The National Center for Atmospheric Research is sponsored by the National Science Foundation.

REFERENCES

Batchelor, G. K., 1967: *An Introduction to Fluid Dynamics.* Cambridge University Press, 615 pp.

Biasutti, M., and D. S. Battisti, 2001: Low-frequency variability in the tropical Atlantic as simulated by the NCAR climate system model and the CCM3 coupled to a slab ocean model. *J. Climate*, submitted.

Bishop, J. K. B., and W. B. Rossow, 1991: Spatial and temporal variability of global surface solar irradiance. *J. Geophys. Res.*, **96,** 16 839–16 858.

Bryan, K., 1969: A numerical method for the study of the circulation of the World Ocean. *J. Comput. Phys.*, **4,** 347–376.

——, S. Manabe, and R. C. Pacanowski, 1975: A global ocean–atmosphere climate model. Part II: The oceanic circulation. *J. Phys. Oceanogr.*, **5,** 30–46.

Bryden, H. L., and E. C. Brady, 1985: Diagnostic model of the three-dimensional circulation in the upper equatorial Pacific Ocean. *J. Phys. Oceanogr.*, **15,** 1255–1273.

Cane, M. A., and E. S. Sarachik, 1977: Forced baroclinic ocean

motions. Part II: The linear equatorial bounded case. *J. Mar. Res.*, **37,** 355–398.
Carton, J. A., X. Cao, B. S. Giese, and A. M. daSilva, 1996: Decadal and interannual SST variability in the tropical Atlantic Ocean. *J. Phys. Oceanogr.*, **26,** 1165–1175.
Chen, D., A. J. Busalacchi, and L. M. Rothstein, 1994a: The roles of vertical mixing, solar radiation, and wind stress in a model simulation of the sea surface temperature seasonal cycle in the tropical Pacific Ocean. *J. Geophys. Res.*, **99,** 20 345–20 359.
——, L. M. Rothstein, and A. J. Busalacchi, 1994b: A hybrid vertical mixing scheme and its applications to tropical ocean models. *J. Phys. Oceanogr.*, **24,** 2156–2179.
Delecluse, P., M. K. Davey, Y. Kitamura, S. G. H. Philander, M. Suarez, and L. Bengtsson, 1998: Coupled general circulation modeling of the tropical Pacific. *J. Geophys. Res.*, **103,** 14 357–14 374.
Freeland, H. J., P. B. Rhines, and H. T. Rossby, 1975: Statistical observations of the trajectories of neutrally buoyant floats in the North Atlantic. *J. Mar. Res.*, **33,** 383–404.
Gent, P. R., and M. A. Cane, 1989: A reduced gravity, primitive equation model of the upper equatorial ocean. *J. Comput. Phys.*, **81,** 444–480.
——, F. O. Bryan, G. Danabasoglu, S. C. Doney, W. R. Holland, W. G. Large, and J. C. McWilliams, 1998: The NCAR Climate System Model Global Ocean Component. *J. Climate*, **11,** 1287–1306.
Gill, A. E., 1982: *Atmosphere–Ocean Dynamics.* Academic Press, 662 pp.
Griffies, S. M., and R. W. Hallberg, 2000: Biharmonic friction with a Smagorinsky-like viscosity for use in large-scale eddy-permitting ocean models. *Mon. Wea. Rev.*, **128,** 2935–2946.
Grima, N., A. Bentamy, K. Katsaros, Y. Quilfen, P. Delecluse, and C. Levy, 1999: Sensitivity of an oceanic general circulation model forced by satellite wind stress fields. *J. Geophys. Res.*, **104,** 7967–7989.
Hastenrath, S., 1991: *Climate Dynamics of the Tropics.* Kluwer Academic, 488 pp.
Johnson, G. C., and D. W. Moore, 1997: The Pacific subsurface countercurrents and an inertial model. *J. Phys. Oceanogr.*, **27,** 2448–2459.
Kalnay, E., and Coauthors, 1996: The NCEP/NCAR 40-Year Reanalysis Project. *Bull. Amer. Meteor. Soc.*, **77,** 437–471.
Large, W. G., and P. R. Gent, 1999: Validation of vertical mixing in an equatorial ocean model using large eddy simulations and observations. *J. Phys. Oceanogr.*, **29,** 449–464.
——, J. C. Williams, and S. C. Doney, 1994: Oceanic vertical mixing: A review and a model with a nonlocal boundary layer parameterization. *Rev. Geophys.*, **32,** 363–403.
——, G. Danabasoglu, S. C. Doney, and J. C. McWilliams, 1997: Sensitivity to surface forcing and boundary layer mixing in a global ocean model: Annual mean climatology. *J. Phys. Oceanogr.*, **27,** 2418–2447.
Latif, M., D. Anderson, T. Barnett, M. Cane, R. Kleeman, A. Leetmaa, J. J. O'Brien, A. Rosati, and E. Schneider, 1998: A review of the predictability and prediction of ENSO. *J. Geophys. Res.*, **103,** 14 375–14 394.
Levitus, S., and T. P. Boyer, 1994: *World Ocean Atlas 1994.* Vol. 4: *Temperature*. NOAA Atlas NESDIS 4, U.S. Department of Commerce, Washington, D.C., 117 pp.
——, R. Burgett, and T. P. Boyer, 1994: *Salinity.* Vol. 3, *World Ocean Atlas 1994.* National Oceanic and Atmospheric Administration, 99 pp.
Love, A. E. H., 1944: *A Treatise on the Mathematical Theory of Elasticity.* Dover, 643 pp.
Luyten, J. R., and D. H. Roemmich, 1982: Equatorial currents at semi-annual period in the Indian Ocean. *J. Phys. Oceanogr.*, **12,** 406–413.
Maes, C., G. Madec, and P. Delecluse, 1997: Sensitivity of an equatorial Pacific OGCM to the lateral diffusion. *Mon. Wea. Rev.*, **125,** 958–971.
McPhaden, M. J., 1982: Variability of the central equatorial Indian Ocean. Part I: Ocean dynamics. *J. Mar. Res.*, **40,** 157–176.
——, and Coauthors, 1998: The Tropical Ocean–Global Atmosphere observing system. *J. Geophys. Res.*, **103,** 14 169–14 240.
McWilliams, J. C., 1996: Modeling the oceanic general circulation. *Annu. Rev. Fluid Mech.*, **23,** 215–248.
——, and J. H. S. Chow, 1981: Equilibrium geostrophic turbulence. Part I: A reference solution in a β-plane channel. *J. Phys. Oceanogr.*, **11,** 921–949.
——, and Coauthors, 1983: The local dynamics of eddies in the western North Atlantic. *Eddies in Marine Science*, A. R. Robinson, Ed., Springer-Verlag, 92–113.
Miles, J., 1994: On transversely isotropic eddy viscosity. *J. Phys. Oceanogr.*, **24,** 1077–1079.
Miller A. J., J. M. Oberhuber, N. E. Graham, and T. M. Barnett, 1992: Tropical Pacific Ocean response to observed winds in a layered general circulation model. *J. Geophys. Res.*, **97,** 7317–7340.
Milliff, R. F., W. G. Large, J. Morzel, G. Danabasoglu, and T. M. Chin, 1999: Ocean general circulation model sensitivity to forcing from scatterometer winds. *J. Geophys. Res.*, **104,** 11 337–11 358.
Munk, W. H., 1950: On the wind driven ocean circulation. *J. Meteor.*, **7,** 79–93.
Pacanowski, R. C., and S. G. H. Philander, 1981: Parameterization of vertical mixing in numerical models of the tropical oceans. *J. Phys. Oceanogr.*, **11,** 1443–1451.
——, and S. M. Griffies, 1998: MOM 3.0 manual. NOAA/GFDL, 668 pp. [Available from NOAA/Geophysical Fluid Dynamics Laboratory, Princeton, NJ 08542.]
——, K. Dixon, and A. Rosati, 1991, 1993: The GFDL modular ocean model users guide. GFDL Ocean Group Tech. Rep. 2. [Available from NOAA/GFDL, Princeton, NJ 08542.]
Philander, S. G. H., 1990: *El Niño, La Niña, and the Southern Oscillation.* Academic Press, 289 pp.
——, and R. C. Pacanowski, 1984: Simulation of the seasonal cycle in the tropical Atlantic Ocean. *Geophys. Res. Lett.*, **11,** 802–804.
——, W. J. Hurlin, and A. D. Siegel, 1987: Simulation of the seasonal cycle of the tropical Pacific Ocean. *J. Phys. Oceanogr.*, **17,** 1986–2002.
Rosati, A., and K. Miyakoda, 1988: A general circulation model for upper ocean simulation. *J. Phys. Oceanogr.*, **18,** 1601–1626,
Rossow, W. B., and R. A. Schiffer, 1991: ISCCP cloud data products. *Bull. Amer. Meteor. Soc.*, **72,** 2–20.
Schudlich, R. R., and J. F. Price, 1992: Diurnal cycles of current, temperature, and turbulent dissipation in a model of the equatorial upper ocean. *J. Geophys. Res.*, **97,** 5409–5422.
Smagorinsky, J., 1963: General circulation experiments with the primitive equations. *Mon. Wea. Rev.*, **91,** 99–164.
Smith, R. D., M. E. Maltrud, F. O. Bryan, and M. W. Hecht, 2000: Numerical simulation of the North Atlantic Ocean at $\frac{1}{10}^\circ$. *J. Phys. Oceanogr.*, **30,** 1532–1561.
Stockdale, T. N., A. J. Busalacchi, D. E. Harrison, and R. Seager, 1998: Ocean modeling for ENSO. *J. Geophys. Res.*, **103,** 14 325–14 356.
Wacongne, S., 1989: Dynamical regimes of a fully nonlinear stratified model of the Atlantic Equatorial Undercurrent. *J. Geophys. Res.*, **94,** 4801–4815.
Wajsowicz, R. C., 1993: A consistent formulation of the anisotropic stress tensor for use in models of the large-scale ocean circulation. *J. Comput. Phys.* **105,** 333–338.
Weaver, A. J., and E. S. Sarachik, 1991: Reply. *J. Phys. Oceanogr.*, **21,** 1702–1707.
Webster, P. J., V. O. Magana, T. N. Palmer, J. Shukla, R. A. Tomas, M. Yani, and T. Yasunari, 1998: Monsoons: Processes, predictability, and the prospects for prediction. *J. Geophys. Res.*, **103,** 14 451–14 510.
Weisberg, R. H., and C. Colin, 1986: Equatorial Atlantic Ocean tem-

perature and current variations during 1983 and 1984. *Nature,* **322,** 240–243.
Williams, G. P., 1972: Friction term formulation and convective instability in a shallow atmosphere. *J. Atmos. Sci.,* **29,** 870–876.
Wyrtki, K., and B. Kilonsky, 1984: Mean water and current structure during the Hawaii to Tahiti shuttle experiment. *J. Phys. Oceanogr.,* **14,** 242–254.
Xie, P., and P. A. Arkin, 1996: Analyses of global monthly precipitation using gauge observations, satellite estimates, and numerical model predictions. *J. Climate,* **9,** 840–858.